vapor, violating the time invariance of the vapor density. Since the diffusive flux of water vapor goes as $1/r^2$, the water vapor density ρ_v must go like a constant plus $1/r$. Given the known water vapor densities at $r = a$ and $r = b = \infty$, this implies that

$$\rho_v(r) = \rho_v(\infty) + \frac{a}{r}[\rho_v(a) - \rho_v(\infty)]. \tag{1}$$

The outward radial diffusive flux is $-k_d \partial \rho_v / \partial r$, where k_d is the diffusivity of water vapor in air. Multiplying that flux by $4\pi r^2$, we get a rate of water vapor mass diffusing outward (evaporation if positive and condensation if negative) equal to $4\pi k_d a[\rho_v(a) - \rho_v(\infty)]$. To focus the discussion on condensation, we may take minus of this expression, giving

$$\text{rate of condensation onto a } \textbf{droplet} = 4\pi k_d a[\rho_v(\infty) - \rho_v(a)], \tag{2}$$

which is proportional to the droplet's radius a, not to the droplet's surface area. Letting $N(a)$ be the number per volume of droplets with radii less than a, it follows that the condensation per volume in a cloud is proportional to the "diameter concentration" $[2\int da(dN/da)a$; Romps et al. 2023] or, equivalently, proportional to the "integral radius" $[\int da(dN/da)a$; Politovich and Cooper 1988; Korolev and Mazin 2003]. The condensation is not proportional to the surface area per volume $[4\pi\int da(dN/da)a^2]$.

For drops and larger droplets (diameters $\gtrsim 100$ μm), sedimentation of the drop can thin the diffusive boundary layer, leading to b/a that cannot be treated as much larger than one. In fact, sedimentation will cause the thickness of the boundary layer to depend on the angle from the stagnation point, but we can still gain valuable insight while approximating the boundary layer as spherically symmetric. Repeating the derivation with general b, we get

$$\text{rate of condensation onto a } \textbf{drop} \approx 4\pi k_d a \frac{\delta + a}{\delta}[\rho_v(b) - \rho_v(a)], \tag{3}$$

where $\delta \equiv b - a$ is the thickness of the boundary layer and where we have used an approximate equality in a nod to our continued assumption of spherical symmetry. For $\delta \gg a$, we recover Eq. (2) and the "proportional to radius" scaling, as expected. On the other hand, if $\delta \ll a$, we get

$$\text{rate of condensation onto a } \textbf{large drop} \approx 4\pi a^2 \frac{k_d}{\delta}[\rho_v(b) - \rho_v(a)], \tag{4}$$

and we see that the condensation rate is proportional to the surface area of the drop and inversely proportional to the thickness of the diffusive boundary layer.

Equations (2)–(4) illustrate why the intuition from our macroscopic world does not apply to microscopic droplets. For macroscopic objects—like a lake, a puddle, or even a large raindrop—the diffusive boundary layer is thin compared to the size of the object, so the total diffusion of water vapor is proportional to the surface area divided by the thickness of the diffusive boundary layer. For microscopic objects, the diffusive boundary layer is large compared to the object, so the water vapor must diffuse through concentric shells of greatly varying area (from $4\pi b^2$ to $4\pi a^2$), and that geometry causes the total diffusion rate to scale with the object's linear size, not its area. For a more rigorous treatment of the departures from proportional to radius or of the effective radius of a nonspherical object, see discussions of ventilation factors and capacitance in Pruppacher and Klett (1978).

It is important to emphasize that nothing written above is novel. As far back as a century ago, experiments showed that a droplet evaporates at a rate in proportion to its radius (Morse 1910; Houghton 1933; Birdi et al. 1989). The theoretical derivation of this phenomenon was first given by Maxwell (1877), although he did not draw attention to the scaling with radius and did not apply the theory to droplets. Since then, the proportionality to radius has been rederived independently at least twice (Langmuir 1918; Houghton 1933) and can now be found in textbooks (e.g., Johnson 1954; Fuchs 1959; Pruppacher and Klett 1978; Rogers and Yau 1989; McFarquhar 2022).

A counterargument to the proportional to radius result is that its derivation assumes a diffusive boundary layer in steady state. In fact, anomalies in evaporation or condensation can scale like the droplet's surface area for a short period of time following an instantaneous disturbance. For example, consider a sudden change at $t = 0$ in the droplet's temperature, which would alter the saturation vapor density at its surface. Immediately afterward, the concentric shell of water vapor affected by this disturbance, which grows diffusively, would have a thickness of $\sqrt{k_d t}$. For $\sqrt{k_d t}$ much less than the droplet radius a, the droplet's spherical geometry does not influence the evolution, and so the transient evaporation/condensation anomaly should, indeed, scale like a^2 during this time period, but this time period is fleeting. The transient signal starts to feel the spherical geometry once $\sqrt{k_d t}$ is comparable to a (i.e., once $\delta \approx 1$), which makes a^2/k_d the time scale over which the condensation or evaporation transitions to scaling like a instead of a^2. For $k_d = 2.5 \times 10^{-5}$ m^2 s^{-1} and a in the range of 1–50 μm, this gives a time scale of 0.04–100 μs. These are time scales that have no relevance to cloud dynamics. Therefore, for all practical purposes, the evaporation or condensation on a small-to-medium-sized droplet may be treated as always proportional to its radius.

Consequently, the typical approach to modeling droplets is to use ordinary differential equations (ODEs), which already assume that condensation and evaporation are proportional to the droplet radius (Howell 1949; Kraus and Smith 1949; Mordy 1959; Neiburger and Chien 1960; Korolev and Mazin 2003). Here, we will evaluate this approximation numerically using a set of partial differential equations (PDEs) for the distribution of water vapor and temperature around a condensing droplet.

2. Model

The governing partial differential equations we will use here are

capacity of dry air at constant pressure, the heat capacity of the droplet is orders of magnitude smaller than the heat capacity of its surrounding air. Therefore, the droplet's heat capacity can be set to zero without any substantial loss of accuracy.

Let us define a droplet's "region of influence" to be the air inside the cloud that is closest to it. For simplicity, we will model that region of influence as spherical. Furthermore, since the thickness of the droplet's diffusive boundary layer b is much larger than the droplet's radius a, we may model b as though it were equal to the radius of influence. We can do this for the same reason that we could earlier take b to be infinite. Henceforth, we will model the droplet's region of influence as dominated by diffusion and conduction (as opposed to advection), letting b represent both the thickness of the diffusive boundary layer and the radius of the region of influence. Using $b^3 \gg a^3$, the masses of a droplet and its region of influence are $4\pi\rho_l a^3/3$ and $4\pi\rho_a b^3/3$, respectively. Since their ratio is q_l, we get $b = a(\rho_l/q_l\rho_a)^{1/3}$, which allows us to initialize b given an initial a and q_l.

Equations (8)–(17) govern the evolution of $\rho_a(r, t)$, $\rho_v(r, t)$, $T(r, t)$, $u(r, t)$, $a(t)$, and $b(t)$. It is self-evident how to evolve most of these in time, but it is less obvious for u. To solve for u, we can use $p = R_a\rho_a T$ to rewrite $\rho_a c_{va} T$ in Eq. (10) in terms of p, which is independent of r, and rearrange to get an explicit expression for $\partial_r(r^2 u)$. Integrating that expression in r starting from a, we get the solution for $u(r, t)$:

$$u(r, t) = \frac{a^2}{r^2}u(a, t) - \frac{c_{va}}{c_{pa}}\frac{r^3 - a^3}{3r^2}\frac{\partial_t p}{p} - \frac{R_a}{c_{pa}}\frac{k_c}{p}\left(\partial_r T - \frac{a^2}{r^2}\partial_r T|_{r=a}\right). \tag{18}$$

For $r \gg a$, this gives

$$u(r, t) \approx -\frac{c_{va}}{c_{pa}}\frac{r}{3}\frac{\partial_t p}{p}, \tag{19}$$

where we have used the fact that $\partial_r T \approx 0$ for $r \gg a$. Plugging this into the continuity equation for ρ_a and integrating, this tells us that $\rho_a \propto p^{c_{va}/c_{pa}}$, which is the expected relationship between density and mass for adiabatic changes in pressure.

In practice, the numerical integration of Eqs. (8)–(17) is performed by splitting diffusion and advection into sequential processes. In the diffusive process, the equations

$$\partial_t \rho_v = \frac{k_d}{r^2}\partial_r(r^2\partial_r\rho_v), \tag{20}$$

$$\partial_t(\rho_a c_{va} T) = \frac{k_c}{r^2}\partial_r(r^2\partial_r T), \tag{21}$$

$$\partial_r\rho_v|_{r=b} = 0, \tag{22}$$

$$\partial_r T|_{r=b} = 0, \tag{23}$$

$$\rho_v(a) = \rho_v^*[T(a)], \text{ and} \tag{24}$$

$$-k_c\partial_r T|_{r=a} = Lk_d\partial_r\rho_v|_{r=a} \tag{25}$$

are integrated over a time step Δt on an Eulerian grid with fixed a and b.

At the end of that diffusive process, $R_a\rho_a T$ is, in general, not equal to $p(t)$ or $p(t + \Delta t)$. In the advective process, we move the gridcell boundaries while conserving the air mass, water vapor mass, and potential temperature of each grid cell. The boundaries are moved such that a matches the new size of the droplet and such that the air in each grid cell is adiabatically compressed or expanded to a pressure of $p(t + \Delta t)$. This calculation is straightforward and fast if the positions of the boundaries are updated sequentially from innermost to outermost. The updated a, b, and intermediate grid boundaries define the Eulerian grid for the next time step. Therefore, although we start a simulation with an initial a and q_l—which together define the initial b—the variables a and b evolve as reflected in the actual movement of the simulation's gridcell boundaries. For more details on the numerical implementation, see appendix B.

In the next section, results are shown from two different types of simulations. In the first, the air is initialized with a uniform temperature and a uniform positive supersaturation (i.e., $S > 0$). In the second type of simulation, the air is initialized with a uniform temperature and a uniform zero supersaturation (i.e., $S = 0$), and then it is depressurized at a rate corresponding to a chosen vertical velocity. The vertical velocity is converted to a change in pressure via the hydrostatic relation using the average density of the simulated air and droplet.

3. Results

To provide a view of the simulation output, we first run a 400-s simulation that is initialized with a droplet of radius $a = 5$ μm in air with a pressure, temperature, and relative humidity of 90 kPa, 290 K, and 1, respectively. The liquid-water mixing ratio q_l is initialized to 10^{-5}, which, assuming the droplets are monodisperse, gives a radius of influence of $b = 2261$ μm. The droplet and its region of influence are lifted at a constant vertical velocity w of 10 m s^{-1}, which is converted to a rate of depressurization at each time step. At 10 m s^{-1} over 400 s, this simulation emulates a cloud ascending adiabatically for 4 km.

Figure 1 zooms in to show the simulation output at small radius (0–50 μm) and small time (0–0.4 s), with the three panels showing, from left to right, the temperature, water vapor density, and supersaturation. The depressurization causes adiabatic changes in temperature far from the droplet: at a radius of 50 μm, the temperature drops by just about 0.04 K, which is as expected for a dry-adiabatic ascent of 4 m. At a radius of 5 μm, however, the temperature drops by less than 0.02 K. This is not because of any thermal inertia of the droplet; recall that liquid water has been simplified to have zero heat capacity. Instead, this is caused by the release of latent heat at the droplet surface. In the middle panel in Fig. 1, this condensation is reflected in the reduction of water vapor density near the droplet surface. Due to diffusion and conduction, those anomalies in temperature and water vapor density are propagating outward. The boundary condition on ρ_v^* and the rapid action of diffusion keep the supersaturation close to zero near the droplet's surface, as can be seen in the right panel in Fig. 1.

Zooming out, Fig. 2 shows the same fields plotted for all radii and the full ascent of 4 km. At this scale, the radial gradients in

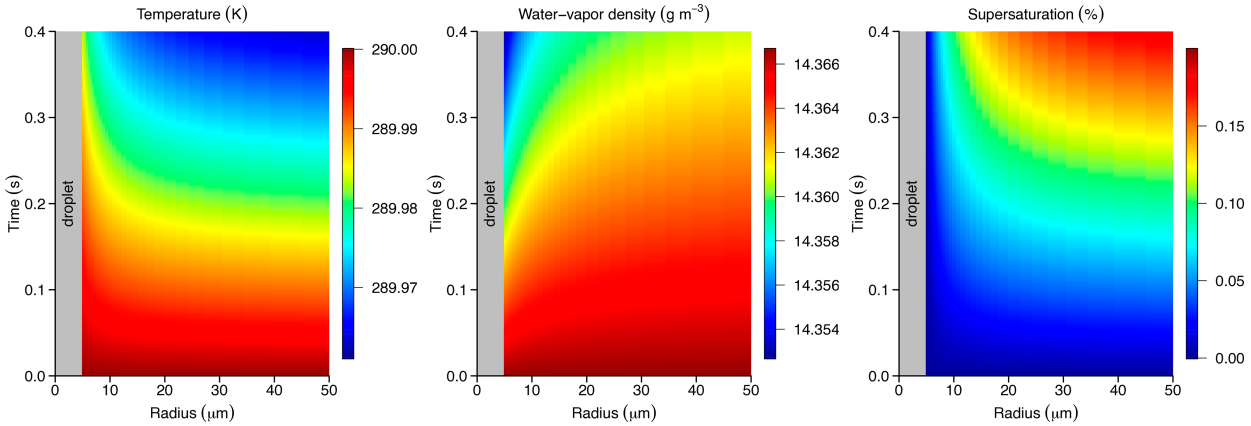

FIG. 1. Zooming into small radii and small time, results for the $w = 10$ m s^{-1} simulation initialized with $a = 5$ μm, $q_l = 10^{-5}$, $p = 90$ kPa, $T = 290$ K, and $S = 0$. Fields of (left) temperature, (middle) water vapor density, and (right) supersaturation are shown for radii up to 50 μm (which is a small fraction of the initial region of influence of $b = 2261$ μm) and for time up to 0.4 s (amounting to 4 m of ascent).

temperature and water vapor are not visible because they are so small compared to the changes with time. Likewise, the 5-μm droplet radius is not visible at the beginning of the simulation but becomes perceptible later in the simulation as the thin gray region; by 400 s, the droplet has grown to $a = 43$ μm.

Among the more noticeable features is the slant to the right edge of the data in the panels in Fig. 2. This is caused by the fact that the concentric layers of air expand as the air depressurizes, causing the radius of influence to increase from $b = 2261$ μm to $b = 2605$ μm. Recall that the interfaces in the simulation are Lagrangian surfaces that move with the dry air.

Note that the change in temperature deviates substantially from a dry-adiabatic lapse rate of 10 K km^{-1}. Given the ascent speed of 10 m s^{-1}, this simulation covers 4 km of ascent, which would cause the temperature to decrease by about 40 K in the absence of condensation. Instead, the temperature decreases by 20 K, which is a mean moist-adiabatic lapse rate of 5 K km^{-1}.

Finally, in the right panel in Fig. 2, we see that the supersaturation peaks just below 6% at 20 s before settling down under 3%. This is an extreme case chosen for illustration. Such large values of supersaturation result from the high vertical velocity (10 m s^{-1}), low cloud droplet number concentration (21 cm^{-3} initially, dropping to 13 cm^{-3} by the end of the simulation due to expansion of the air), and the fact that this model does not nucleate any new droplets.

Recall that the standard ODEs for droplets assume condensation is proportional to the droplet radius. We can check the accuracy of those ODEs using the PDEs presented here, which make no such assumption. Figure 3 shows, in its black curves, a digitized replication of the time series of supersaturation from Fig. 1a of Korolev and Mazin (2003), which were made with the ODEs. The curves represent the mean supersaturation of a cloud initialized at $t = 0$ with $S = 0$ and 200 cm^{-3} of monodisperse droplets with 5-μm radii, ascending at 0.25, 0.5, 1, and 2 m s^{-1}. The blue curves in Fig. 3 are produced from integrating Eq. (14) of Korolev and Mazin (2003)—which combines two ODEs into a single integro-differential equation—with the parameters used in this study. Finally, the red curves are made using this paper's PDEs, where the representative supersaturation S plotted here and in subsequent figures is the mass of water vapor in excess of saturation in the droplet's region of influence, i.e., $(\int_a^b dr r^2 \rho_v)/(\int_a^b dr r^2 \rho_v^*) - 1$.

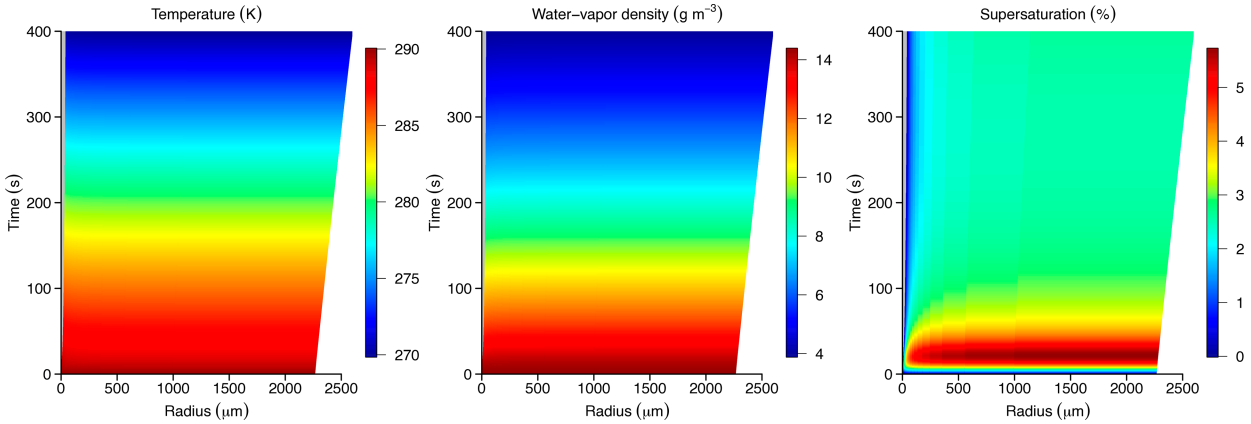

FIG. 2. As in Fig. 1, but showing the fields over all radii for the full 400 s of simulation.

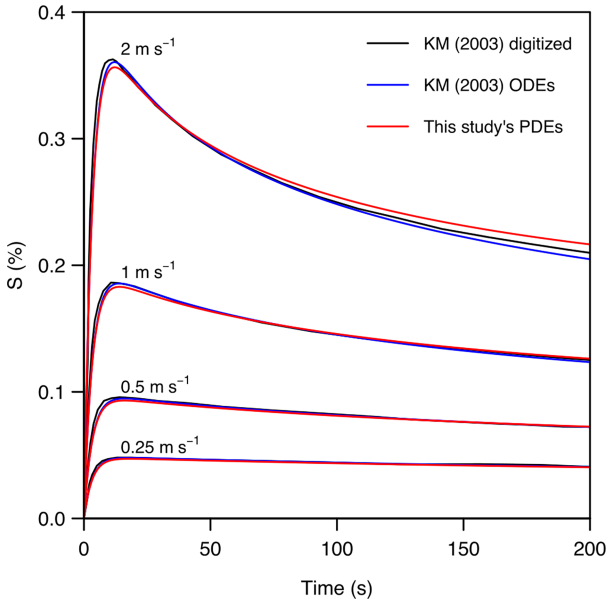

FIG. 3. Time series of mean supersaturation S in a cloud initialized with $S = 0$ and 200 cm^{-3} of monodisperse droplets with 5-μm radii lifted at 0.25, 0.5, 1, and 2 m s^{-1} that have been digitized from Fig. 1a of Korolev and Mazin (2003) (black), calculated from Eq. (14) of Korolev and Mazin (2003) (blue), and calculated using this study's model (red).

For the slow ascent speed of 0.25 m s^{-1} in Fig. 3, the supersaturation adjusts to a quasi-steady value on a time scale of a few seconds and remains approximately constant. For the fast ascent speed of 2 m s^{-1}, there is an adjustment to a quasi-steady supersaturation on the same time scale (Korolev and Mazin 2003) but that quasi-steady value declines with time as the radius of the droplets grows: for a given condensation rate (imposed, e.g., by the rate of ascent), a larger droplet means that a smaller supersaturation is needed to generate that rate. The good agreement between the ODE and PDEs in Fig. 3 validates the ODE approach to modeling supersaturation, which treats condensation as proportional to the droplet radius.

To directly test whether condensation is proportional to droplet area or droplet radius, we can plot the time series of a droplet's latent heating Q (with dimensions of power) divided by either supersaturation times droplet area (Sa^2) or supersaturation times droplet radius (Sa). Here, Q is L times the rate of condensation onto the droplet, i.e., $Q = 4\pi a^2 L k_d \partial_r \rho_v|_{r=a}$. In the two sets of experiments to be used for this test, the droplet and its surroundings are initialized to a total pressure of 90 kPa and a temperature of 290 K, and the PDEs are integrated with a time step of 1 ms.

In the first set of experiments, there is no ascent (i.e., the pressure is held constant at 90 kPa), but the air is initialized with a positive supersaturation. Therefore, the droplet and its environment draw the supersaturation down toward zero while warming up the air by latent heating and growing the size of the droplet. Figure 4 shows the results of these experiments for all eight combinations of initial conditions selected from $a = 5$ or 50 μm, $S = 1\%$ or 10%, and $q_l = 10^{-5}$ or 10^{-4}.

The left panel in Fig. 4 plots time series of Q/Sa^2. The black curves remain fairly constant in time because their droplets ($a = 50$ μm) and regions of influence are relatively large, which means that S, a, and Q do not change appreciably in 10 s. The red curves have droplets ($a = 5$ μm) and regions of influence that are relatively small, so their S, a, and Q do change appreciably in 10 s, causing the red curves to vary noticeably. What is important, however, is that all of these simulations (black and red combined) exhibit a wide range of Q/Sa^2, which means that

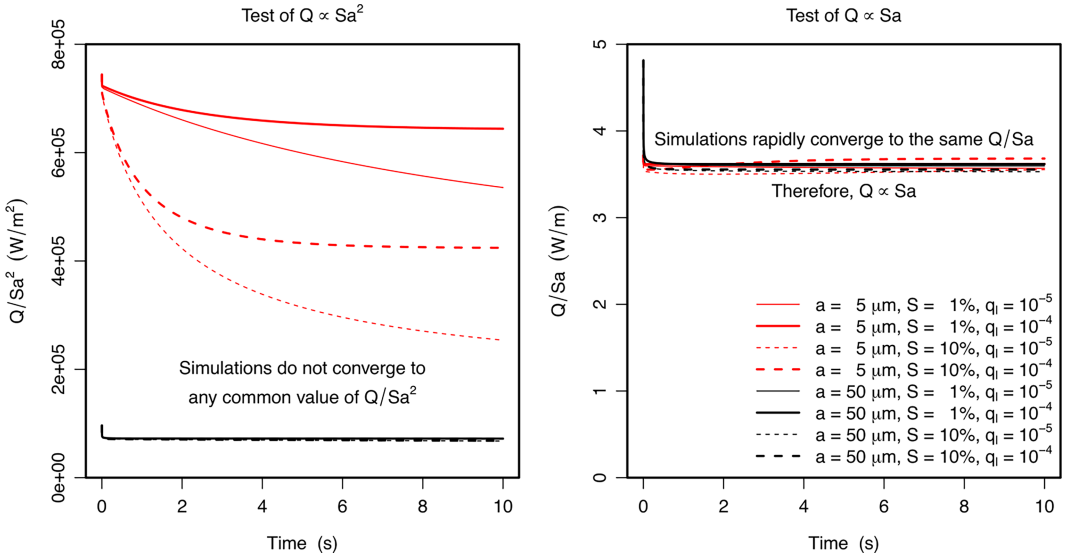

FIG. 4. For zero ascent and positive initial supersaturation, the time series of latent heating Q divided by either (left) Sa^2 or (right) Sa. Time series are shown for all eight combinations of initial conditions: $a = 5$ or 50 μm, $S = 1\%$ or 10%, and $q_l = 10^{-5}$ or 10^{-4}.

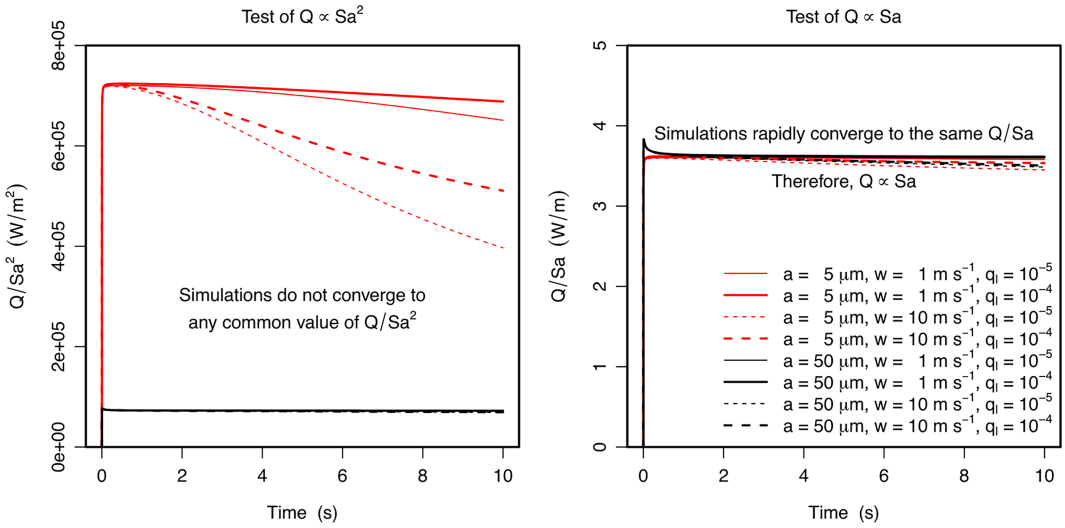

FIG. 5. For positive ascent and zero initial supersaturation, the time series of latent heating Q divided by either (left) Sa^2 or (right) Sa. Time series are shown for all eight combinations of $a = 5$ or 50 μm, $w = 1$ m s^{-1} or 10 m s^{-1}, and $q_l = 10^{-5}$ or 10^{-4}.

there is no proportionality between latent heating and droplet area.

The right panel in Fig. 4 plots time series of Q/Sa. Here, we see that the simulations rapidly converge to a common value of Q/Sa regardless of the initial conditions. This tells us that latent heating Q is proportional to the droplet radius a, i.e., $Q \propto Sa$. In fact, the value of Q/Sa to which these simulations converge can be derived analytically (see Text S5 of Romps et al. 2023). The expression is

$$\frac{Q}{Sa} = 4\pi L\left[\left(\frac{L}{R_v T} - 1\right)\frac{L}{k_c T} + \frac{R_v T}{k_d p_v^*(T)}\right]^{-1}, \tag{26}$$

which is about 3.6 W m^{-1} for $T = 290$ K.

Figure 5 shows the second set of experiments, in which the supersaturation is initially zero, but there is ascent (i.e., the pressure decreases with time). These experiments are of the types that are shown in Figs. 1 and 2. In the left panel in Fig. 5, we see again that there is no consistent relationship between latent heating and droplet area. In the right panel, however, we see that the latent heating quickly snaps to a value of Q/Sa, implying a proportionality between Q and a, i.e., $Q \propto Sa$.

4. Discussion

It has been demonstrated here that the rate of condensation in a warm-phase cloud is proportional to the supersaturation times the sum of droplet radii, not the sum of droplet areas. Equivalently, we may say that the volumetric condensation rate is proportional to the sum of droplet diameters per volume, which Romps et al. (2023) referred to as the diameter concentration. This gives a diagnostic relationship, which can be thought of as holding instantaneously so long as we can neglect the time scale over which droplets and their immediate surroundings adjust to each other. At ~0.04–100 μs, that time scale is safe to ignore when studying cloud dynamics.

As with any diagnostic relationship, it is important not to overinterpret its causality. For example, given two clouds, it is not generally true that the one with the higher diameter concentration will have the higher condensation rate. This is because a cloud's supersaturation adjusts as needed to ensure that the supersaturation remains quasi-steady. The time scale for this adjustment is in the range of ~0.1–10 s for typical warm-phase clouds (Squires 1952; Politovich and Cooper 1988; Korolev and Mazin 2003). This has been called the "time of phase relaxation" (Korolev and Mazin 2003), but a more descriptive name might be the "supersaturation-adjustment time scale." Consider, for example, a cloud that suddenly starts rising at some speed. Beyond the supersaturation-adjustment time scale, there is a balance between the declining mass fraction of water vapor caused by condensation and the decreasing saturation mass fraction caused by cooling of the cloud; this occurs with whatever quasi-steady supersaturation is required to achieve the balance. This is why the moist-adiabatic lapse rate is largely independent of the speed of ascent or the size distribution of droplets. For most purposes, the moist-adiabatic lapse rate can be approximated as independent of those details.

Therefore, beyond the saturation-adjustment time scale of ~0.1–10 s, the condensation rate is set by the cloud's vertical velocity, not by its diameter concentration. In fact, in this quasi-steady limit, we can derive an explicit expression for S in which it is proportional to the product of the diameter concentration $2\int da(dN/da)a$ and the vertical velocity w (Squires 1952). That approximation to the actual supersaturation is referred to as the quasi-steady supersaturation; see Text S5 of Romps et al. (2023) for a derivation. Differences between the quasi-steady supersaturation and the actual supersaturation

are due, primarily, to uncertainties in whether the observed cloud has been in steady ascent longer than the time scale of supersaturation adjustment. Since moist-convective updrafts—appropriately defined—live much longer than the saturation-adjustment time scale, the quasi-steady supersaturation is a good proxy for the actual supersaturation in numerical simulations (Romps et al. 2023) and has been relied on as a proxy for supersaturation in observational studies (Warner 1968; Politovich and Cooper 1988; Prabha et al. 2011; Siebert and Shaw 2017; Romps et al. 2023).

It is important to note that the validity of the quasi-steady supersaturation depends on the fact that latent heating is proportional to the droplet radius, but the "proportional to radius" result does not depend on a cloud having achieved a quasi-steady supersaturation. Whereas the quasi-steady supersaturation is a valid approximation to the supersaturation only for ascent that has been steady longer than the saturation-adjustment time scale, the diagnostic relationship between condensation, supersaturation, and the sum of droplet radii applies to all time scales of relevance to cloud dynamics.

Acknowledgments. This work was supported by the U.S. Department of Energy, Office of Science, Office of Biological and Environmental Research, under Award DE-SC0025214.

Data availability statement. No empirical data were used in this study. The figures are generated using the equations in the manuscript.

APPENDIX A

Sedimentation and Turbulence

The model presented here assumes that the air surrounding the droplet is stationary (aside from expansion and contraction) with respect to the droplet. In reality, the surrounding air has some droplet-relative motion due to droplet sedimentation and turbulent shear. Here, we show that the exclusion of these phenomena does not affect the primary conclusions.

First, we can show that droplet sedimentation operates on a time scale that is long compared to the time scale over which diffusion and conduction generate a scaling of fluxes to the droplet. For Stokes flow, the terminal velocity of the droplet is

$$v_t = \frac{2}{9}\frac{\rho_l/\rho_a - 1}{\nu} g a^2, \tag{A1}$$

where $\nu = \mathrm{Sc} k_d \approx 1.5 \times 10^{-5}\ \mathrm{m^2\ s^{-1}}$ is the kinematic viscosity and Sc = 0.6 is the Schmidt number for water vapor in air. In the lower troposphere, this gives approximately

$$v_t \approx (10^8\ \mathrm{m^{-1}\ s^{-1}}) a^2. \tag{A2}$$

To confirm that the droplet is in the regime of Stokes flow, we can calculate the Reynolds number $\mathrm{Re} = 2 a v_t/\nu$. For a = 1–50 μm, this is about 10^{-5}–1. Since this is less than or equal to one, Stokes flow is a good approximation. The time scale for the droplet to fall a distance equal to its radius is then $a/v_t = (10^{-8}\ \mathrm{m\ s})/a$. For a = 1–50 μm, this is a time scale of 10 000–200 μs. This can be compared to the time scale it takes to establish a scaling, which, for a = 1–50 μm, was calculated to be 0.04–100 μs in section 1. We see that the sedimentation time scale is much longer than the time scale of adjustment to a scaling. Therefore, droplet sedimentation would not alter the conclusions if it were included in the model.

Second, we can show that the shear from turbulence operates on a length scale that is large compared to the droplet radius a and on a time scale that is long compared to the adjustment to a scaling. For a high dissipation rate of turbulent kinetic energy around 0.1 $\mathrm{m^2\ s^{-3}}$, the Kolmogorov microscale $\eta = (\nu^3/\varepsilon)^{1/4}$ is about 500 μm, which is much larger than the radii of small-to-medium droplets (a of 1–50 μm). The Kolmogorov time scale is $\sqrt{\nu/\varepsilon} \approx 10$ ms, which is much longer than the time scale of adjustment to a scaling, which we have calculated to be 0.04–100 μs. Therefore, turbulent shear would not alter the conclusions if it were included in the model.

APPENDIX B

Model Integration

The radial coordinate r has its origin at the center of the droplet, as depicted in Fig. B1. The first grid interface is at $r = r_1(t) \equiv a(t)$, where a denotes the droplet's radius. The outermost interface level is at $r = r_{N+1}(t) \equiv b(t)$, where N is the number of concentric shells of air and b is the radius of the droplet's region of influence given by $b = a(\rho_l/q_l\rho_a)^{1/3}$.

For simplicity, water is restricted to vapor and liquid only, and both phases are treated as having zero heat capacity. Mathematically, the zero heat capacity of liquid water forces the fluxes of sensible and latent heat at the droplet surface to be equal and opposite. Physically, we can think of the droplet as having a very low heat capacity with a temperature (or, at least, skin temperature) that is equal to that of the air immediately around it.

In the model, the concentric shells of air around the droplet are labeled with integers 1 through N, with shell i bounded by interfaces i and $i + 1$, as depicted in Fig. B1. Each shell i has a temperature T_i, dry-air density $\rho_{a,i}$, and a water vapor density $\rho_{v,i}$. The volume of shell i is $V_i = (4\pi/3)(r_{i+1}^3 - r_i^3)$, and the mass of dry air in shell i, given by $\rho_{a,i}V_i$, is time invariant. The flows of water vapor $F_{v,i}$ and sensible heat $F_{T,i}$ through interface i are positive when pointing in the direction of increasing radius.

Recall that the time integration is split into a diffusive process (with diffusion of heat and moisture, but no movement of grid interfaces) and an advective process (with no diffusion of heat and moisture, but the grid interfaces move to equilibrate the pressure). The equations governing the diffusive process are

$$V_i \frac{d\rho_{v,i}}{dt} = F_{v,i} - F_{v,i+1}, \tag{B1}$$

$$V_i \rho_{a,i} c_{va} \frac{dT_i}{dt} = F_{T,i} - F_{T,i+1}, \tag{B2}$$

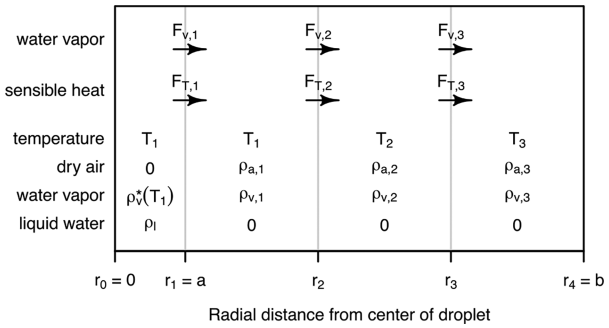

FIG. B1. Example of a one-dimensional finite-volume grid for the simulation of spherically symmetric three-dimensional diffusion and conduction through $N = 3$ concentric air layers.

where c_{va} is the specific heat capacity of dry air at constant volume. The heat capacity at constant volume is used here (instead of at constant pressure) because, within a single time step, the diffusion and conduction process is performed at constant volume. The fluxes used here are

$$F_{v,i} = \begin{cases} 4\pi r_1^2 k_d \dfrac{\rho_v^*[T_1(0)] + \rho_v^{*\prime}[T_1(0)]\{T_1 - T_1(0)\} - \rho_{v,1}}{(r_2 - r_1)/2} & i = 1 \\ 4\pi r_i^2 k_d \dfrac{\rho_{v,i-1} - \rho_{v,i}}{(r_{i+1} - r_{i-1})/2} & i \in [2, N] \\ 0 & i = N + 1. \end{cases}$$

$$F_{T,i} = \begin{cases} -LF_{v,1} & i = 1 \\ 4\pi r_i^2 k_c \dfrac{T_{i-1} - T_i}{(r_{i+1} - r_{i-1})/2} & i \in [2, N] \\ 0 & i = N + 1, \end{cases} \tag{B3}$$

where L is the specific latent heat of evaporation and $k_c = 2.5 \times 10^{-2}$ W m^{-1} K^{-1} is the thermal conductivity of air. Here, we have Taylor expanded the saturation water density $\rho_v^*(T_1)$ to first order in T_1 with $T_1(0)$ being, in the numerical implementation, the initial value of T_1 at the beginning of the time step.

The initial values of r_i are chosen to be a stretched grid to resolve all of the relevant dynamics. There are $N = 40$ shells in total with the first shell having a thickness of about $0.05a$. Because the grid spacing is so fine, these equations cannot be solved using an explicit integration method without incurring a large computational cost. For example, a grid spacing of $0.05a$ for $a = 5$ μm generates a diffusion time scale of $(0.05a)^2/k_d = 2.5$ ns. Since a nanosecond time step is not practical, the system of equations is linearized at each time step, allowing the fast processes to be integrated efficiently using matrix exponentiation. This is why the dependence of ρ_v^* on temperature has been Taylor expanded in the equations above.

Using $\rho_{v,i}$ and T_i as the prognostic variables, and stacking them into a vector $\mathbf{X}^{\mathrm{T}} = (\rho_v, T)$, the matrix equation is

$$\frac{d\mathbf{X}}{dt} = \mathbf{A}\mathbf{X} + \mathbf{B}, \tag{B4}$$

where the nonzero elements of matrix $\mathbf{A}$ are

$$\mathbf{A}_{1,1} = -\frac{8\pi k_d}{V_1}\left(\frac{r_1^2}{r_2 - r_1} + \frac{r_2^2}{r_3 - r_1}\right), \tag{B5}$$

$$\mathbf{A}_{1,2} = \frac{8\pi k_d}{V_1}\frac{r_2^2}{r_3 - r_1}, \tag{B6}$$

$$\mathbf{A}_{1,N+1} = \frac{8\pi k_d}{V_1}\frac{r_1^2}{r_2 - r_1}\rho_v^{*\prime}[T_1(0)], \tag{B7}$$

$$\mathbf{A}_{i,i-1} = \frac{8\pi k_d}{V_i}\frac{r_i^2}{r_{i+1} - r_{i-1}} \quad \text{for } i \in [2, N-1], \tag{B8}$$

$$\mathbf{A}_{i,i} = -\frac{8\pi k_d}{V_i}\left(\frac{r_i^2}{r_{i+1} - r_{i-1}} + \frac{r_{i+1}^2}{r_{i+2} - r_i}\right) \quad \text{for } i \in [2, N-1], \tag{B9}$$

$$\mathbf{A}_{i,i+1} = \frac{8\pi k_d}{V_i}\frac{r_{i+1}^2}{r_{i+2} - r_i} \quad \text{for } i \in [2, N-1], \tag{B10}$$

$$\mathbf{A}_{N,N-1} = \frac{8\pi k_d}{V_N}\frac{r_N^2}{r_{N+1} - r_{N-1}}, \tag{B11}$$

$$\mathbf{A}_{N,N} = -\frac{8\pi k_d}{V_N}\frac{r_N^2}{r_{N+1} - r_{N-1}}, \tag{B12}$$

$$\mathbf{A}_{N+1,N+1} = -\frac{8\pi k_c}{V_1\rho_{a,1}c_{va}}\left\{\frac{k_d}{k_c}L\frac{r_1^2}{r_2 - r_1}\rho_v^{*\prime}[T_1(0)] + \frac{r_2^2}{r_3 - r_1}\right\}, \tag{B13}$$

$$\mathbf{A}_{N+1,N+2} = \frac{8\pi k_c}{V_1\rho_{a,1}c_{va}}\frac{r_2^2}{r_3 - r_1}, \tag{B14}$$

$$\mathbf{A}_{N+1,1} = \frac{8\pi k_c}{V_1\rho_{a,1}c_{va}}\frac{k_d}{k_c}L\frac{r_1^2}{r_2 - r_1}, \tag{B15}$$

$$\mathbf{A}_{N+i,N+i-1} = \frac{8\pi k_c}{V_i\rho_{a,i}c_{va}}\frac{r_i^2}{r_{i+1} - r_{i-1}} \quad \text{for } i \in [2, N-1], \tag{B16}$$

$$\mathbf{A}_{N+i,N+i} = -\frac{8\pi k_c}{V_i\rho_{a,i}c_{va}}\left(\frac{r_i^2}{r_{i+1} - r_{i-1}} + \frac{r_{i+1}^2}{r_{i+2} - r_i}\right) \quad \text{for } i \in [2, N-1], \tag{B17}$$

$$\mathbf{A}_{N+i,N+i+1} = \frac{8\pi k_c}{V_i\rho_{a,i}c_{va}}\frac{r_{i+1}^2}{r_{i+2} - r_i} \quad \text{for } i \in [2, N-1], \tag{B18}$$

$$\mathbf{A}_{2N,2N-1} = \frac{8\pi k_c}{V_N\rho_{a,N}c_{va}}\frac{r_N^2}{r_{N+1} - r_{N-1}}, \tag{B19}$$

$$\mathbf{A}_{2N,2N} = -\frac{8\pi k_c}{V_N\rho_{a,N}c_{va}}\frac{r_N^2}{r_{N+1} - r_{N-1}}, \tag{B20}$$

and the only nonzero elements of $\mathbf{B}$ are

$$\mathbf{B}_1 = \frac{8\pi k_d}{V_1}\frac{r_1^2}{r_2 - r_1}\{\rho_v^*[T_1(0)] - \rho_v^{*\prime}[T_1(0)]T_1(0)\}, \quad \text{(B21)}$$

$$\mathbf{B}_{N+1} = -\frac{8\pi k_c}{V_1\rho_{a,1}c_{va}}\frac{k_d}{k_c}L\frac{r_1^2}{r_2 - r_1}\{\rho_v^*[T_1(0)] - \rho_v^{*\prime}[T_1(0)]T_1(0)\}. \quad \text{(B22)}$$

In the advective process, r_1 (also known as a) is updated to make the radius of the droplet consistent with its new mass (based on the amount of water vapor diffused to or away from the droplet in the diffusive process). Then, r_2 is updated (while conserving the masses and potential temperature of the air in that first concentric shell) to give a pressure in the first concentric shell equal to the externally specified pressure. This step is repeated, sequentially, for r_3 to r_N (also known as b), at which point the time step is complete.

REFERENCES

Ackerman, A. S., O. B. Toon, and P. V. Hobbs, 1995: Numerical modeling of ship tracks produced by injections of cloud condensation nuclei into marine stratiform clouds. *J. Geophys. Res.*, **100**, 7121–7133, https://doi.org/10.1029/95JD00026.

Birdi, K. S., D. T. Vu, and A. Winter, 1989: A study of the evaporation rates of small water drops placed on a solid surface. *J. Phys. Chem.*, **93**, 3702–3703, https://doi.org/10.1021/j100346a065.

Chen, Q., I. Koren, O. Altaratz, R. H. Heiblum, G. Dagan, and L. Pinto, 2017: How do changes in warm-phase microphysics affect deep convective clouds? *Atmos. Chem. Phys.*, **17**, 9585–9598, https://doi.org/10.5194/acp-17-9585-2017.

——, J. Fan, Y. Yin, and B. Han, 2020: Aerosol impacts on mesoscale convective systems forming under different vertical wind shear conditions. *J. Geophys. Res. Atmos.*, **125**, e2018JD030027, https://doi.org/10.1029/2018JD030027.

Cotton, W. R., 2024: Aerosol-induced invigoration of cumulus clouds—A review. *Atmosphere*, **15**, 924, https://doi.org/10.3390/atmos15080924.

Cui, Z., K. S. Carslaw, Y. Yin, and S. Davies, 2006: A numerical study of aerosol effects on the dynamics and microphysics of a deep convective cloud in a continental environment. *J. Geophys. Res.*, **111**, D05201, https://doi.org/10.1029/2005JD005981.

Dagan, G., I. Koren, and O. Altaratz, 2015: Competition between core and periphery-based processes in warm convective clouds—From invigoration to suppression. *Atmos. Chem. Phys.*, **15**, 2749–2760, https://doi.org/10.5194/acp-15-2749-2015.

——, ——, ——, and R. H. Heiblum, 2017: Time-dependent, non-monotonic response of warm convective cloud fields to changes in aerosol loading. *Atmos. Chem. Phys.*, **17**, 7435–7444, https://doi.org/10.5194/acp-17-7435-2017.

Deng, L., L. Xue, W. Huang, W. Wu, G. Thompson, W. Gao, N. Sarkadi, and I. Geresdi, 2024: A numerical investigation of aerosol effect on cloud microphysics in an idealized tropical cyclone using the WRF piggybacking framework. *Atmos. Res.*, **304**, 107422, https://doi.org/10.1016/j.atmosres.2024.107422.

Duce, R. A., S. Yuk-Bon, and J. L. Moyers, 1969: Variation of sodium and chloride concentrations with rainfall intensity in Hawaiian trade wind showers. *Pac. Sci.*, **23**, 483–495.

Efraim, A., and Coauthors, 2022: Satellite-based detection of secondary droplet activation in convective clouds. *J. Geophys. Res. Atmos.*, **127**, e2022JD036519, https://doi.org/10.1029/2022JD036519.

Fan, J., and Z. Li, 2022: Aerosol interactions with deep convective clouds. *Aerosols and Climate*, K. S. Carslaw, Elsevier, 571–617.

——, and Coauthors, 2018: Substantial convection and precipitation enhancements by ultrafine aerosol particles. *Science*, **359**, 411–418, https://doi.org/10.1126/science.aan8461.

——, Y. Zhang, Z. Li, J. Hu, and D. Rosenfeld, 2020: Urbanization-induced land and aerosol impacts on sea-breeze circulation and convective precipitation. *Atmos. Chem. Phys.*, **20**, 14 163–14 182, https://doi.org/10.5194/acp-20-14163-2020.

Fuchs, N. A., 1959: *Evaporation and Droplet Growth in Gaseous Media* (in Russian). Pergamon Press, 72 pp.

Gao, W., C.-H. Sui, J. Fan, Z. Hu, and L. Zhong, 2016: A study of cloud microphysics and precipitation over the Tibetan Plateau by radar observations and cloud-resolving model simulations. *J. Geophys. Res. Atmos.*, **121**, 13 735–13 752, https://doi.org/10.1002/2015JD024196.

Houghton, H. G., 1933: A study of the evaporation of small water drops. *Physics*, **4**, 419–424, https://doi.org/10.1063/1.1745155.

Howell, W. E., 1949: The growth of cloud drops in uniformly cooled air. *J. Meteor.*, **6**, 134–149, https://doi.org/10.1175/1520-0469(1949)006<0134:TGOCDI>2.0.CO;2.

Johnson, J. C., 1954: *Physical Meteorology*. The Technology Press of the Massachusetts Institute of Technology and John Wiley & Sons, Inc., 393 pp.

Koren, I., G. Dagan, and O. Altaratz, 2014: From aerosol-limited to invigoration of warm convective clouds. *Science*, **344**, 1143–1146, https://doi.org/10.1126/science.1252595.

——, O. Altaratz, and G. Dagan, 2015: Aerosol effect on the mobility of cloud droplets. *Environ. Res. Lett.*, **10**, 104011, https://doi.org/10.1088/1748-9326/10/10/104011.

Korolev, A. V., and I. P. Mazin, 2003: Supersaturation of water vapor in clouds. *J. Atmos. Sci.*, **60**, 2957–2974, https://doi.org/10.1175/1520-0469(2003)060<2957:SOWVIC>2.0.CO;2.

Kraus, E. B., and B. Smith, 1949: Theoretical aspects of cloud drop distributions. *Aust. J. Sci. Res.*, **2**, 376–388, https://doi.org/10.1071/CH9490376.

Langmuir, I., 1918: The evaporation of small spheres. *Phys. Rev.*, **12**, 368, https://doi.org/10.1103/PhysRev.12.368.

Lee, S. S., and J. E. Penner, 2011: Dependence of aerosol–cloud interactions in stratocumulus clouds on liquid-water path. *Atmos. Environ.*, **45**, 6337–6346, https://doi.org/10.1016/j.atmosenv.2011.08.050.

——, ——, and M. Wang, 2009: Comparison of a global-climate model simulation to a cloud-system resolving model simulation for long-term thin stratocumulus clouds. *Atmos. Chem. Phys.*, **9**, 6497–6520, https://doi.org/10.5194/acp-9-6497-2009.

——, L. J. Donner, and J. E. Penner, 2010: Thunderstorm and stratocumulus: How does their contrasting morphology affect their interactions with aerosols? *Atmos. Chem. Phys.*, **10**, 6819–6837, https://doi.org/10.5194/acp-10-6819-2010.

——, and Coauthors, 2021: Midlatitude mixed-phase stratocumulus clouds and their interactions with aerosols: How ice processes affect microphysical, dynamic, and thermodynamic development in those clouds and interactions? *Atmos. Chem. Phys.*, **21**, 16 843–16 868, https://doi.org/10.5194/acp-21-16843-2021.

Leung, W.-Y. H., and Coauthors, 2016: Sensitivity of a continental night-time stratocumulus-topped boundary layer to varying environmental conditions. *Quart. J. Roy. Meteor. Soc.*, **142**, 2911–2924, https://doi.org/10.1002/qj.2877.

Li, X., Y. Pan, Z. Mo, and R. Liu, 2022: Aerosol invigoration effect in Guilin (China). *Atmos. Sci. Lett.*, **23**, e1077, https://doi.org/10.1002/asl.1077.

Lkhamjav, J., H. Lee, Y.-L. Jeon, J. M. Seo, and J.-J. Baik, 2018: Impacts of aerosol loading on surface precipitation from deep convective systems over North Central Mongolia. *Asia-Pac. J. Atmos. Sci.*, **54**, 587–598, https://doi.org/10.1007/s13143-018-0080-5.

Madhulatha, A., J. Dudhia, R.-S. Park, S. C. Bhan, and M. Mohapatra, 2023: Effect of single and double moment microphysics schemes and change in cloud condensation nuclei, latent heating rate structure associated with severe convective system over Korean peninsula. *Atmosphere*, **14**, 1680, https://doi.org/10.3390/atmos14111680.

Maxwell, J. C., 1877: Diffusion. *Encyclopaedia Britannica*, Vol. VII, 9th ed. Adam and Charles Black, 214–221.

McFarquhar, G. M., 2022: Rainfall microphysics. *Rainfall*, R. Morbidelli, Eds., Elsevier, 1–26, https://doi.org/10.1016/B978-0-12-822544-8.00009-3.

Mordy, W., 1959: Computations of the growth by condensation of a population of cloud droplets. *Tellus*, **11A**, 16–44, https://doi.org/10.1111/j.2153-3490.1959.tb00003.x.

Morse, H. W., 1910: On evaporation from the surface of a solid sphere. Preliminary note. *Proc. Amer. Acad. Arts Sci.*, **45**, 363–367, https://doi.org/10.2307/20022561.

Neiburger, M., and C. W. Chien, 1960: Computations of the growth of cloud drops by condensation using an electronic digital computer. *Physics of Precipitation: Proceedings of the Cloud Physics Conference, Woods Hole, Massachusetts, June 3–5, 1959, Wiley Online Library*. *Geophys. Monogr.*, Vol. **5**, Amer. Geophys. Union, 191–210.

Park, J. M., and S. C. van den Heever, 2022: Weakening of tropical sea breeze convective systems through interactions of aerosol, radiation, and soil moisture. *Atmos. Chem. Phys.*, **22**, 10 527–10 549, https://doi.org/10.5194/acp-22-10527-2022.

Patade, S., and Coauthors, 2019: Role of liquid phase in the development of ice phase in monsoon clouds: Aircraft observations and numerical simulations. *Atmos. Res.*, **229**, 157–174, https://doi.org/10.1016/j.atmosres.2019.06.022.

Petters, J. L., H. Jiang, G. Feingold, D. L. Rossiter, D. Khelif, L. C. Sloan, and P. Y. Chuang, 2013: A comparative study of the response of modeled non-drizzling stratocumulus to meteorological and aerosol perturbations. *Atmos. Chem. Phys.*, **13**, 2507–2529, https://doi.org/10.5194/acp-13-2507-2013.

Politovich, M. K., and W. A. Cooper, 1988: Variability of the supersaturation in cumulus clouds. *J. Atmos. Sci.*, **45**, 1651–1664, https://doi.org/10.1175/1520-0469(1988)045<1651:VOTSIC>2.0.CO;2.

Prabha, T. V., A. Khain, R. S. Maheshkumar, G. Pandithurai, J. R. Kulkarni, M. Konwar, and B. N. Goswami, 2011: Microphysics of premonsoon and monsoon clouds as seen from in situ measurements during the Cloud Aerosol Interaction and Precipitation Enhancement Experiment (CAIPEEX). *J. Atmos. Sci.*, **68**, 1882–1901, https://doi.org/10.1175/2011JAS3707.1.

Pruppacher, H. R., and J. D. Klett, 1978: *Microphysics of Clouds and Precipitation.* Atmospheric and Oceanographic Sciences Library, Vol. 18, D. Reidel Pub. Co., 714 pp.

Rogers, R. R., and M. K. Yau, 1989: *A Short Course in Cloud Physics.* 3rd ed. Butterworth-Heinemann, 304 pp.

Romps, D. M., 2021: The Rankine–Kirchhoff approximations for moist thermodynamics. *Quart. J. Roy. Meteor. Soc.*, **147**, 3493–3497, https://doi.org/10.1002/qj.4154.

——, K. Latimer, Q. Zhu, T. Jurkat-Witschas, C. Mahnke, T. Prabhakaran, R. Weigel, and M. Wendisch, 2023: Air pollution unable to intensify storms via warm-phase invigoration. *Geophys. Res. Lett.*, **50**, e2022GL100409, https://doi.org/10.1029/2022GL100409.

Rosenfeld, D., 2018: Cloud-aerosol-precipitation interactions based of satellite retrieved vertical profiles of cloud microstructure. *Remote Sensing of Aerosols, Clouds, and Precipitation*, T. Islam et al., Eds., Elsevier, 129–152.

——, and Coauthors, 2023: Frontiers in satellite-based estimates of cloud-mediated aerosol forcing. *Rev. Geophys.*, **61**, e2022RG000799, https://doi.org/10.1029/2022RG000799.

Roy, P., R. M. Rauber, and L. Di Girolamo, 2024: Evolution of cloud droplet temperature and lifetime in spatiotemporally varying subsaturated environments with implications for ice nucleation at cloud edges. *Atmos. Chem. Phys.*, **24**, 11 653–11 678, https://doi.org/10.5194/acp-24-11653-2024.

Seigel, R. B., S. C. van den Heever, and S. M. Saleeby, 2013: Mineral dust indirect effects and cloud radiative feedbacks of a simulated idealized nocturnal squall line. *Atmos. Chem. Phys.*, **13**, 4467–4485, https://doi.org/10.5194/acp-13-4467-2013.

Sheffield, A. M., S. M. Saleeby, and S. C. van den Heever, 2015: Aerosol-induced mechanisms for cumulus congestus growth. *J. Geophys. Res. Atmos.*, **120**, 8941–8952, https://doi.org/10.1002/2015JD023743.

Siebert, H., and R. A. Shaw, 2017: Supersaturation fluctuations during the early stage of cumulus formation. *J. Atmos. Sci.*, **74**, 975–988, https://doi.org/10.1175/JAS-D-16-0115.1.

Squires, P., 1952: The growth of cloud drops by condensation. I. General characteristics. *Aust. J. Sci. Res.*, **5**, 59–86, https://doi.org/10.1071/CH9520059.

Stier, P., and Coauthors, 2024: Multifaceted aerosol effects on precipitation. *Nat. Geosci.*, **17**, 719–732, https://doi.org/10.1038/s41561-024-01482-6.

Vaillancourt, P. A., M. K. Yau, and W. W. Grabowski, 2001: Microscopic approach to cloud droplet growth by condensation. Part I: Model description and results without turbulence. *J. Atmos. Sci.*, **58**, 1945–1964, https://doi.org/10.1175/1520-0469(2001)058<1945:MATCDG>2.0.CO;2.

Warner, J., 1968: The supersaturation in natural clouds. *J. Rech. Atmos.*, **3**, 233–237.

Wu, Y., and Y. Peng, 2022: Investigation of aerosol effects on a deep convection case in southeast China with budget analysis of hydrometeor mass and latent heat. *Atmos. Res.*, **277**, 106275, https://doi.org/10.1016/j.atmosres.2022.106275.

Zhang, Y., J. Fan, Z. Li, and D. Rosenfeld, 2021: Impacts of cloud microphysics parameterizations on simulated aerosol–cloud interactions for deep convective clouds over Houston. *Atmos. Chem. Phys.*, **21**, 2363–2381, https://doi.org/10.5194/acp-21-2363-2021.

Zhou, X., N. Bei, H. Liu, J. Cao, L. Xing, W. Lei, L. T. Molina, and G. Li, 2017: Aerosol effects on the development of cumulus clouds over the Tibetan Plateau. *Atmos. Chem. Phys.*, **17**, 7423–7434, https://doi.org/10.5194/acp-17-7423-2017.